# Chapter-4

## Combustion Synthesized $KNiPO_4$: A Non-Toxic, Robust, Intercalating Battery-type Pseudocapacitive Electrode for Hybrid Supercapacitors as a Large-scale Energy Storage Solutions

## 4.1 Introduction

In search to develop superior electrodes for hybrid supercapacitors, polyanionic framework type material containing $(XO_4)^{n-}$ tetrahedron ( where X= P, S, As, Si) that is covalently bonded with M-O polyhedral (Where M= Fe, Ni, Mn, Co, Ti, V, Cr ) linkage are envisaged as robust electrode due to their open pore structure that enables fast ion transport during charge-discharge and active participation of $M^{n/n+1}$ redox couple. In this chapter, we are reporting Potassium Nickel phosphate ($KNiPO_4$) as a potential robust electrode for the hybrid capacitor to be employed to power the implantable biomedical devices as well as become a choice of electrode for large-scale grid-level energy storage and delivery solutions due to its long cyclic life and stable energy storage performances. Initial Electrochemical measurement has been performed on a three-electrode system, and $KNiPO_4$ showed excellent charge storage performance achieving energy density 168.5 mAh/g (Capacitance: 935 F/g) at a current density of 1A/g in an aqueous 2M KOH electrolyte. Two electrodes are assembled $KNiPO_4$ vs. Activated carbon, and the electrochemical result shows the capacity of 242.6 mAh/g (Capacitance: 546 F/g) at a current rate of 1A/g in 2M aqueous KOH electrolyte. The manuscript presents the synthesis, characterizations, and a detailed investigation of the electrochemical charge storage performances of the electrode.

## 4.2 Experimental Procedure

### 4.2.1 Synthesis of $KNiPO_4$

$KNiPO_4$ was synthesized by the modified solution combustion process followed by calcination of precipitate at elevated temperature to get the crystalline material. Analytical grade precursors were used for synthesis without any further purification. Deionized water (DI) (resistivity = 18.0 MΩ, pH = 7) was utilized for solution preparation for the entire

study. By taking 1 mM of Nickel acetate (Merck 99.0%), 1mM of potassium acetate (Merck 99.0%), and 1 mM of Ammonium phosphate (Merck 99.0%), cation solution was prepared in 100 ml of DI water. Then 1 mM of citric acid was added drop by drop in the cation solution to form a homogeneous metal citrate complex at 100 ºC. Both the solutions were mixed with continuous stirring for 4 hours at 100 ºC resulting in the green gel formation. Thereafter, the temperature of the gel was raised to 400ºC; the gel solution got boiled after that and ignited, followed by burning with a glowing flame. The entire combustion process took place for about ~3 min yielding voluminous fluffy brown materials. The materials were ground and kept in a muffle furnace at 650ºC for 5 hours. The pinkish brown or light brown colored powder was collected from the crucible and ground adequately and utilized for further characterization and electrochemical performance study.

### 4.2.2 Materials characterization

The purity and crystallinity of the compound were examined by powder XRD study using the benchtop powder X-ray diffractometer (Rigaku miniflex 600) with Cu Kα radiation (λ = 1.54056 Å) in 10-60º 2θ range of with a step size equal to 0.02. The structure was matched with X'Pert High Score Plus (PANalytical); further crystal structure of the materials was refined by the Rietveld refinement method using FullProf Suite software. The morphological study of the material was examined by EVO - Scanning Electron Microscope MA15 / 18 CARL ZEISS and FT-IR spectra were measured in the wavenumber range of 450–4000 $cm^{-1}$ to understand the functional group present in the material with FT-IR spectrometer (Nicolet 6700, Thermo scientific. The elemental composition and their electronic states were examined by (K-Alpha Thermo scientific) X-ray photoelectron spectrometer. The surface area and pore size distribution of the sample were studied using a BET surface area analyzer (BELSORP-II, Microtrac BEL Japan) with the help of $N_2$ adsorption/ desorption isotherms at 77 K.

Electrochemical performances of the electrode by cyclic voltammetry (CV), galvanostatic charge-discharge (GCD), and electrochemical impedance spectroscopy (EIS) were studied by the conventional three-electrode system and measured by Metrohm Autolab (PGSTAT204) coupled with a FRA32M module for impedance analysis. NOVA1.1 software was used to analyze the Electrochemical measurements.

### 4.2.3 Electrode preparation

Working $KNiPO_4$ electrode was prepared in a 70:20:10 weight % of the active material ($KNiPO_4$), Conducting carbon (Acetylene black, Alfa Aesar), and binder (PVDF, Merck) respectively in NMP: N-Methyl-2-pyrrolidone solvent. The homogenous slurry was made using an agate mortar pestle, and slurry containing ~1 mg of active material was coated over a Toray carbon paper (Alfa Aesar) in a working surface area of 1 $cm^2$. Drying of the as-prepared electrode was done at 80$^oC$ for 12 hours. Thereafter, the weight of the loaded electrode material was calculated by taking the difference between the weight of the material loaded electrode and the weight of the blank electrode (Shimadzu electronic weighing balance machine, error limit: 0.01 mg). As prepared, dried electrodes were used for further study of electrochemical measurement. In a three-electrode arrangement, Hg/HgO (1M KOH) was used as the reference electrode, and platinum plate as the counter electrode. In full cell (Hybrid supercapacitor Mode), electrochemical studies were performed using the Activated Carbon as the counter cum reference electrode in 2M KOH electrolyte.

## 4.3 Results and discussion

The crystal structure of $KNiPO_4$ (calcined at 650 °C for 5 h) was determined by powder XRD study and from the XRD peak profile matches with reference peak (JCPDS No.: 25-0582). Rietveld refined the XRD profile of calcined $KNiPO_4$ shown in **Fig. 4.1-(a), which** matched well reference structure with no observation of any impurity peaks. Refined cell

parameters (a = 8.6348, b= 9.2623, c= 4.9105) and $R_p$= 9.94, $R_{wp}$= 8.37, $R_{exp}$ = 4.15, $\chi^2$= 4.06 represent the Orthorhombic Crystal structure formation with space group pna21. **VESTA** image shown in **Fig. 4.1-(b)** confirm the presence of Phosphate ($PO_4^{3-}$) tetrahedral connected by corner sharing with 5 coordinated Ni-O polyhedra. **Fig. 4.1-(c)** shows the FTIR spectrum of $KNiPO_4$ powder samples between the wavenumber range of 400-4000$cm^{-1}$. In the FTIR spectra, a strong band arose at 1054.83 due to asymmetric stretching($\nu_{as}$) of P-O bond vibration (990-1200$cm^{-1}$), and symmetric stretching($\nu_{ss}$) vibration of P-O results in strong transmittance peak at 982.3$cm^{-1}$, 943$cm^{-1}$ (900-990cm-1) of -$PO_4$ group [1-2]. Peaks at 630.1 and 574.41 referred to O-P-O out-plane bending, and vibrational peaks at 536.94 and 488.51 arise due to in-plane bending vibration of the O-P-O bond of -$PO_4$ group [3-4]. Thus, the major vibrational spectra validate the presence of the -$PO_4$ group in $KNiPO_4$.

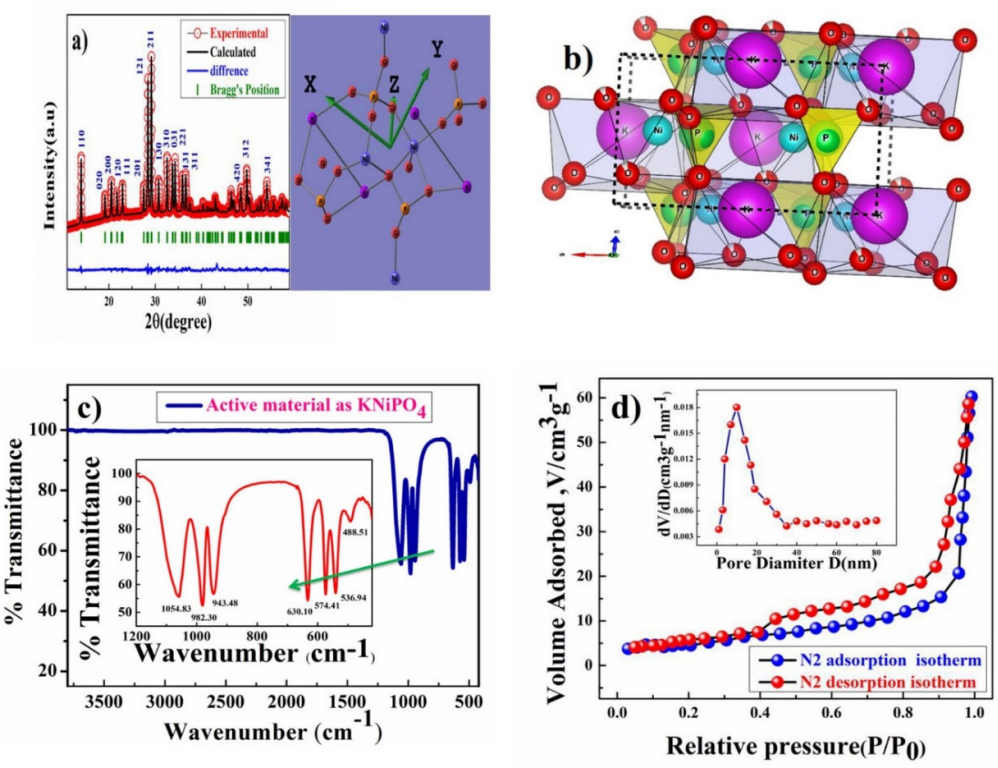


***Figure 4.1*** *(a) XRD Rietveld refinement pattern of $KNiPO_4$ powder sample (b) VESTA image of $KNiPO_4$ (c) FTIR spectrum of $KNiPO_4$ (d) $N_2$ adsorption/desorption isotherm of KNiPO4 sample*

Furthermore, to analyze the surface area and pore volume of the sample, the $N_2$ adsorption-desorption isotherm obtained at 77k is shown in **Fig. 4.1(d)** and it represents the type IV isotherm with the hysteresis loop of H3 type [5]. Monolayer adsorption occurs up to relative pressure ($P/P_o$) < 0.3, here, both adsorption and desorption isotherm overlap each other, i.e., reversible in this region. While in the relative pressure $0.3<(P/P_o)<1.0$, there is a lack of saturation indicating the mesoporous and multilayer adsorption with a specific surface area of the sample equivalent to 54.6 $m^2/g$ with major pore size distribution in a range of 5 to 12 nm is obtained by BJH (Brunauer, Joyner, and Halenda) plot (inset of **Fig. 4.1(d)**). Mesopores are attributed to result in good electrochemical performance of the materials because of high porosity. The calculated average pore diameter of the $KNiPO_4$ sample was found to be ~5.72 nm.

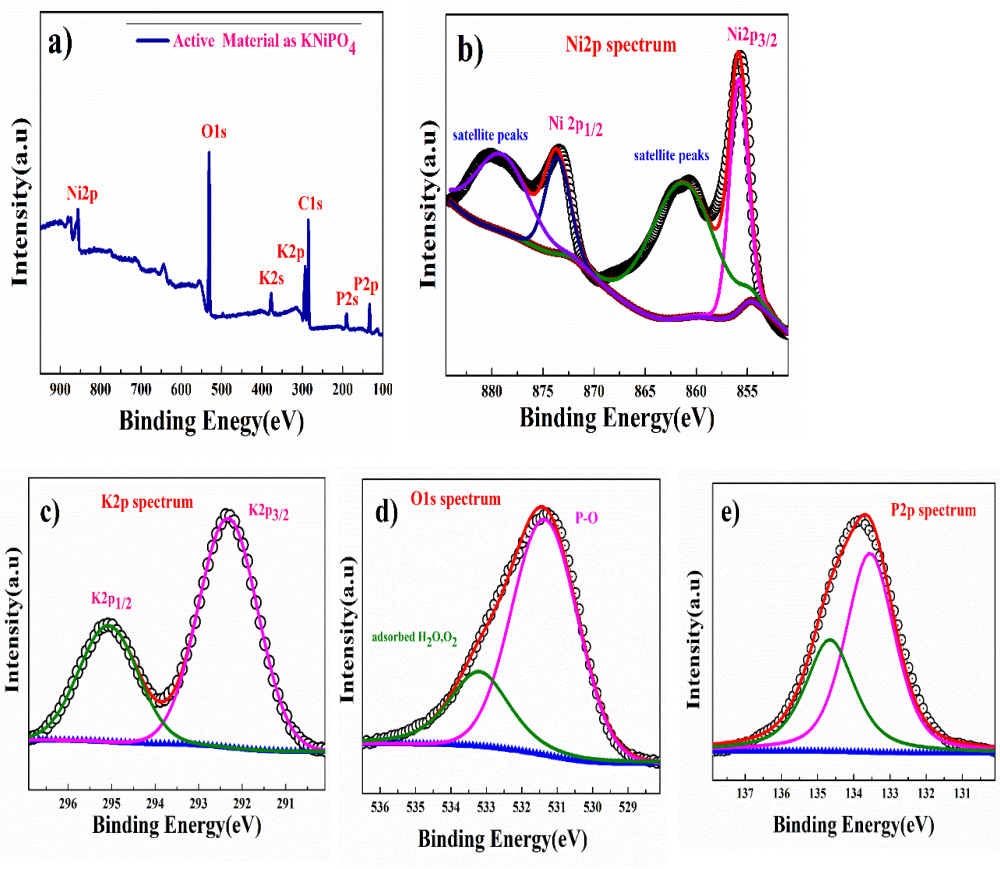


***Figure 4.2*** *XPS of $KNiPO_4$ of powder sample; (a) full survey, (b) Ni(2p), (c) K (1s), (d) O (1s) and (e) P (2p)*

The chemical composition and oxidation state of KNiPO4 were examined using the XPS (X-ray photoelectron spectroscopy). The complete survey spectrum presented in **Fig. 4.2(a)** confirms the presence of K, Ni, P, and O in the sample. The core level spectrum of Ni(2p) is shown in **Fig. 4.2(b)** and is deconvoluted into Ni 2p3/2 and Ni 2p1/2 states at the binding energies of 855.5 eV and 873.4 eV respectively, with corresponding satellite peaks at 860.9eV and 879 eV.

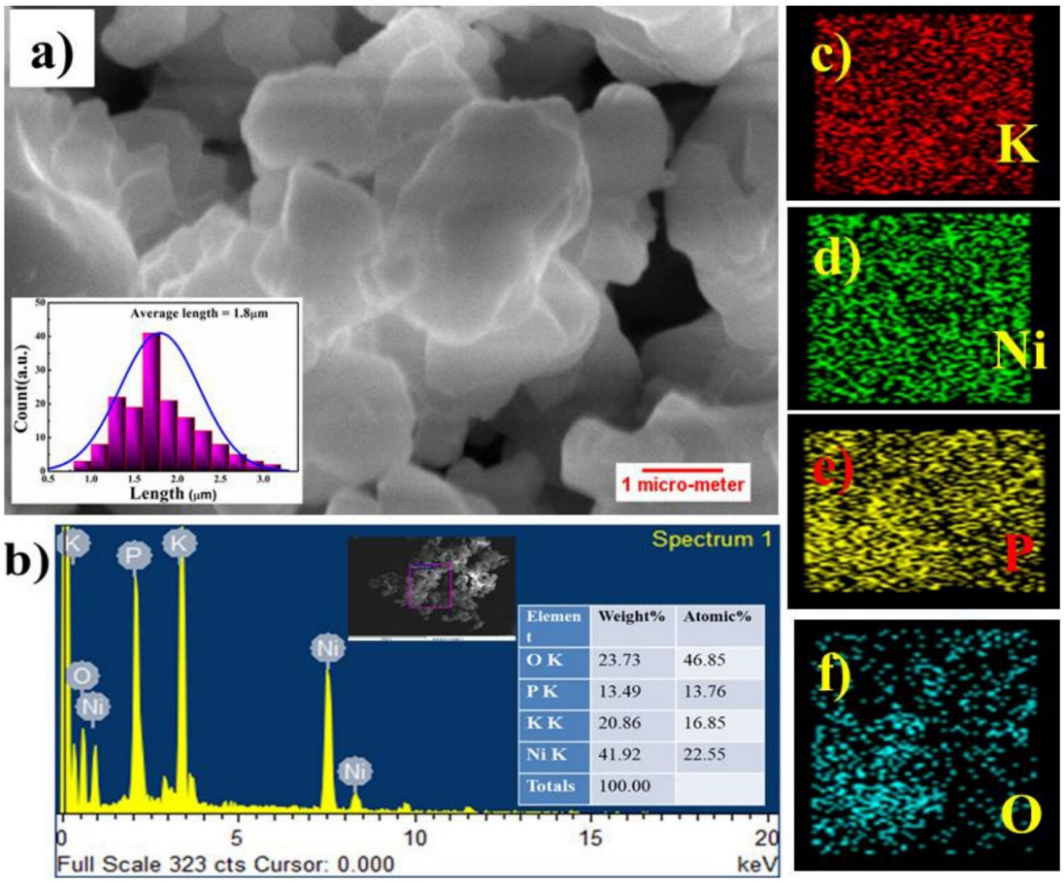


***Figure 4.3*** *(a) Particle distribution of $KNiPO_4$ in SEM image, (b) elemental analysis of $KNiPO_4$ by EDX, and (c-f) showing the elemental mapping of K, Ni, P, O respectively*

**Fig. 4.3(a)** represents the SEM image of the sample displaying the particle morphology and surface structure of the $KNiPO_4$ power sample suggesting the few micrometer sizes of Particles in flakes-like arrangements. Elemental analysis of the $KNiPO_4$ sample is shown in **Fig. 4.3(b) in** the form of an Energy Dispersive X-ray Analysis (EDX) image that confirms

the elemental composition of the material. **Fig. 4.3(c-f)** presents the elemental mapping of K, Ni, P, and O in the sample respectively that confirm the uniform distribution of the elements in the sample.

High-resolution transmission electron microscopy (HRTEM) images of the $KNiPO_4$ sample are shown in **Fig. 4.4 (a)** represents the lattice fringes of the sample and **Fig. 4.4 (a) (i-ii)** represents the FFT (fast Furrier transformation) and inverse FFT image. **Fig. 4.4 (b)** shows the thickness of lattice fringes as the calculated d spacing (408 nm) matches very well with the (120) plane of the $KNiPO_4$ lattice. Lattice fringes of this region presented in the inverse fast Fourier transform (FFT) mapping with Gatan Digital micrograph software confirm the crystalline nature of the sample.

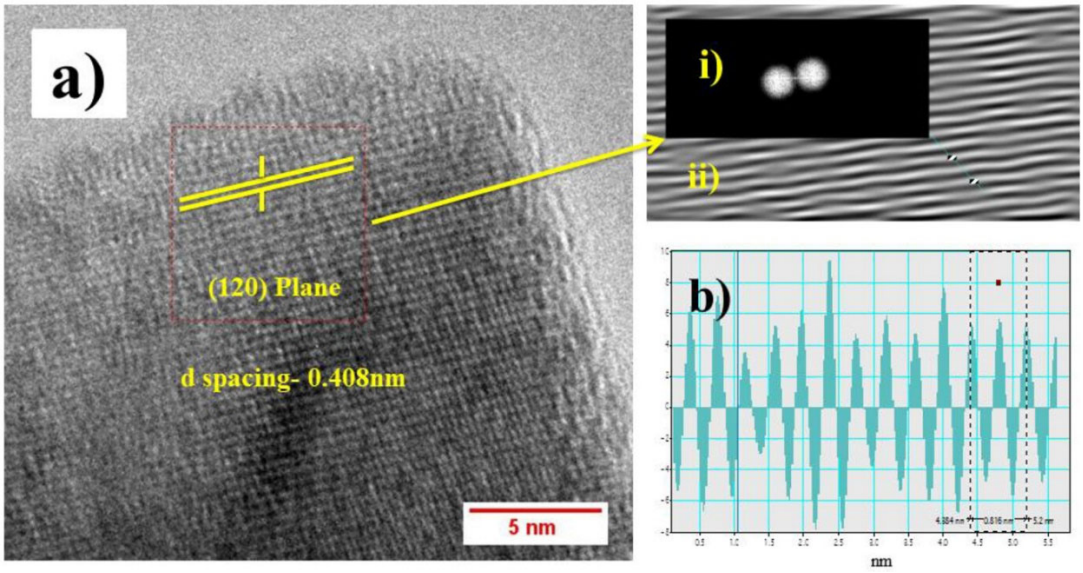


***Figure 4.4 (a)*** *visible lattice fringes containing 120 planes in HR-TEM image,* ***(i-ii):*** *FFT and inverse FFT images of the selected region of the (120) plane. (b) shows d spacing of fringes that matches with the (120) plane of the $KNiPO_4$ lattice.*

### 4.3.1 Electrochemical Studies

The electrochemical performance of $KNiPO_4$ as the working electrode was examined in the three-electrode arrangement where $KNiPO_4$ was utilized as a working electrode, saturated Hg/HgO (1M KOH) as reference electrode, and a Platinum plate was used as a counter

electrode in 2M KOH as an electrolyte. The redox behaviour of $KNiPO_4$ was characterized using a Cyclic-voltammetry (CV) curve between the potential range of 0 V to 0.65 V. **Fig. 4.5(a)** shows the CV curve of $KNiPO_4$; the nature of the curve presents the redox-mediated intercalating storage coupled with surface redox (electrosorption) behaviour. The nature of the CV curve nature confirms the intercalative type of redox-mediated storage. Redox peaks resulted due to the reversible interconversion of $Ni^{2+}$ to $Ni^{3+}$ through Electrosorption of $OH^-$ ion represented by Eq. 4.1 [6-7].

Redox-mediated diffusion-controlled intercalation:

$$KNi((II))PO_4 + OH^-_{sol} \longleftrightarrow KNi(III)(OH^-)PO_4 \quad (4.1)$$

EDLC-type surface capacitance:

$$KNi((II))PO_4 + xKOH \longleftrightarrow K^+_x \mid KNi((II))PO_4 \mid xOH^- \quad (4.2)$$

Total charge storage capacity:

$$KNi((II))PO_4 + xKOH + OH^-_{sol} \longleftrightarrow K^+_x \mid KNi((II))PO_4 \mid OH^-_{(1+x)} \quad (4.3)$$

Using the CV curve, the charge storage capacity of the materials can also be calculated using equation 2 to analyze the electrochemical characteristics of the working electrode [7,8, 9].

$$\mathrm{Csp} = \frac{\int \mathrm{i}\,(\mathrm{V})\mathrm{dV}}{\mathrm{mV}\vartheta} \quad (4.4)$$

The specific charge storage capacity in mAh/g can be calculated using Eq. 4.5.

$$C\left(\frac{mAh}{g}\right) = Csp * \Delta V = \frac{\int i\,(V)dV}{m\vartheta * 3.6} \quad (4.5)$$

Where 'm' is the active mass of the electrode (g), 'V' is the operating voltage window (V), and '$\vartheta$' is the scan rate (mV/s).

The charge storage capacity of $KNiPO_4$ was calculated using Eq. 4.4 & 4.5, and capacity was found close to 121 mAh/g (capacitance: 671F/g) at 1mV/s scan rate.

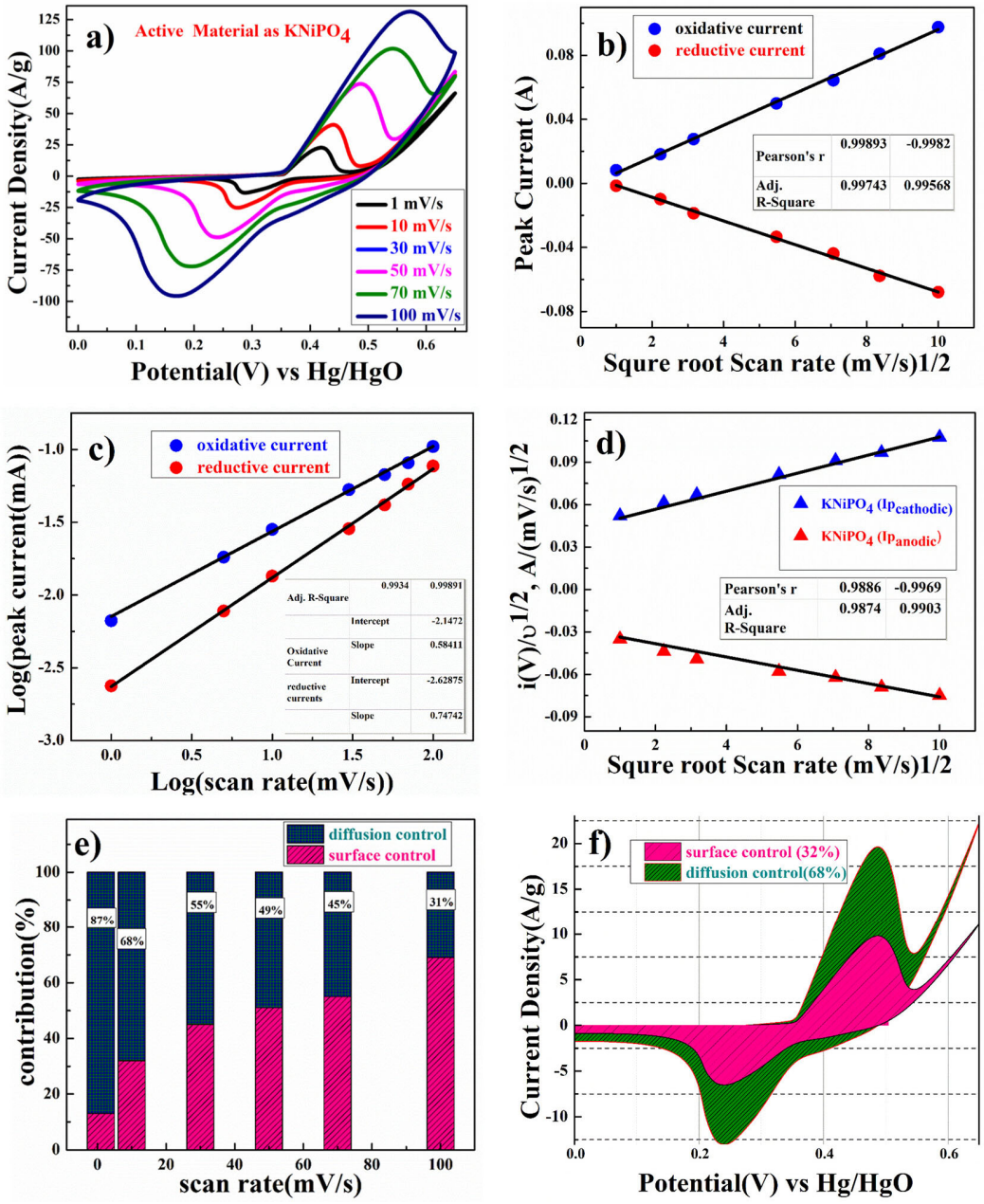


***Figure. 4.5*** *(a) cyclic voltammetry of $KNiPO_4$ electrode in 2 M KOH electrolyte, (b) peak current density vs square root of the scan rates plot, (c) plot of log (peak current) vs log (scan rate) presenting b Values, (d) capacitive and diffusion control process contribution in the current density at the scan rate of 10 mV/s, (e) capacitive and diffusion control process contribution with different scan rates and (f) presenting surface capacitance and diffusion-controlled interaction process contribution at a scan rate 10 mV/s on the charging peak potential equal to 0.49V.*

The shifting of an anodic peak, and the cathodic peak was observed linearly with increasing scan rate confirm the dominance of diffusion-controlled intercalative type of redox-mediated charge storage in the materials. **Fig. 4.5(b)** shows the relation of anodic and

cathodic peak current linearly with the square root of the scan rate, confirming that the $KNiPO_4$ electrode exhibits the semi-infinite diffusion-controlled redox reaction. The Kinetics of electrodes can be examined by determining the ion diffusion coefficient. The ion diffusion coefficient of the electrode was calculated using the Randles-Sevick equation presented below [10-11].

$$i_p = 2.686 \times 10^5 \times n^{3/2} A D^{1/2} C_o v^{1/2} \quad (4.6)$$

Where $i_p$ is peak current density (A), n is the number of electrons that participated in the redox reaction (usually 1), A is the area of the electrode in $cm^2$, D is diffusion coefficient in $cm^2/s$, $C_o$ is $OH^-$ ion concentration in $mol/cm^3$ and ν is scan rate in V/s.

Using Eq. 4.6, the diffusion coefficient of $OH^-$ in the $KNiPO_4$ electrode was found to be $1.13\times10^{-9}$ $cm^2/s$ for the oxidation reaction and $2.31\times10^{-9}$ $cm^2/s$ for the reduction reaction. To qualitatively understand the electrochemical kinetics, a power-law equation was used given below in Eq.4.7 [12].

$$i = a\nu^b \quad (4.7)$$

a and b are adjustable parameters, i is the current (A), and ν is the scan rate (V/s). The b values lie between 0.5 to 1, b equal to 0.5 stands for the intercalative semi-infinite diffusion control redox process or battery-type charge storage behavior, while b equal to 1 represents the surface-controlled charge storage. **Fig. 4.5(c)** shows the log (peak current ($i_p$) vs log (v) plots and from the slope of the plot, b values are extracted. The b-value of current observed for oxidation and reduction was found close to 0.58 and 0.74 respectively, suggesting the superiority of semi-infinite diffusion-controlled intercalating processes resulting in the intercalative redox-mediated charge storage in the electrode [13-14].

**Fig. 4.5(d)** presents the Voltammetry sweep rate dependence on the current density plot that can quantitatively extract the capacitive contribution to the current density. The current

density at a fixed potential is the contribution of both surface capacitive effects and diffusion-controlled insertion process represented by Eq. 4.8 [8,10,15-17].

$$i(\upsilon) = k_1 v + k_2 v^{\frac{1}{2}} \quad (4.8)$$

Eq. 4.8 was simplified into Eq. 4.9 to separate the individual contributions.

$$\frac{i(\upsilon)}{\upsilon^{\frac{1}{2}}} = \frac{k_1}{\upsilon^{\frac{1}{2}}} + k_2 \quad (4.9)$$

From Eq. 4.9**,** $k_1$ and $k_2$ explain the current contributions from the surface capacitive charge storage and the diffusion-controlled intercalative charge storage respectively. Thus, after the extraction of $k_1$ and $k_2$, individual contributions at specific potentials can be quantified. The $k_1$ and $k_2$ are calculated from the slope and intercept of the $i(V)/v^{1/2}$ vs. $v^{1/2}$ plot shown in **Fig. 4.5(d)**. **Fig. 4.5(e)** represents the contribution of surface-controlled charge storage and diffusion- controlled interactive charge storage at different scan rates. As shown in **Fig. 4.5(f)**, after the calculation of k1 and k2 values, the contribution of surface-controlled charge storage was close to 32 %) and the contribution for the diffusion-controlled interaction process was close to 68% at 0.49 V peak potential with 10 mV/s scan rate.

As suggested by Trassati, the total charge storage capacitance of a material is the aggregate of the inner and outer surface contribution to the capacitance of the electrode and is represented by Eq. 4.10 [18,8,10].

$$C_{total} = C_{in} + C_{out} \text{ (F /g)} \quad (4.10)$$

The total charge storage capacitance contribution from the inner and outer surface of the electrode is dependent upon the square root of the scan rate. As shown in **Fig. 4.6(a),** the y-intercept of the linear fit of $C^{-1}$ vs. $v^{1/2}$ at different scan rates shows the total charge stored at the electrode or the total capacitance of the electrode. As shown in **Fig. 4.6(b),** the y-intercept of the linear C vs. $v^{1/2}$ curve exhibits the outer surface contribution to charge storage or outer capacitance ($C_{out}$) of the electrode. Using the Trassati plot, the total

Capacitance value ($C_{total}$) was found close to 121mAh/g (capacitance: 671F/g ) at 1mV/s. inner surface contribution in total capacitance, $C_{in}$ was found to be 70mAh/g or 389 F/g (58 % of total capacity), and outer surface contribution to the total capacitance, $C_{out}$ was found to be 50.8mAh/g (Capacitance: 281 F/g (42 %of total capacity) at the scan rate of 1 mV/s. Galvanostatic charge/discharge studies were performed to get a more realistic and applicable capacitance of the electrode. From the charge-discharge curve, the charge storage capacity (total capacitance) of the electrode can be calculated using Eq. 4.11 [18,8].

$$\mathrm{Csp} = \frac{\mathrm{I}\Delta\mathrm{t}}{\mathrm{m}\Delta\mathrm{V}} \qquad (4.11)$$

The specific capacity of the electrode in mAh/g is calculated by modifying (Eq. 4.11) as represented below.

$$C\left(\frac{mAh}{g}\right) = Csp * \Delta V = \frac{I\Delta t}{m*3.6} \qquad (4.12)$$

Where I is the discharge current density (A), Δt is the discharge time (s), m is the active mass of the electrode (g) and ΔV is the potential window of the discharge (V).

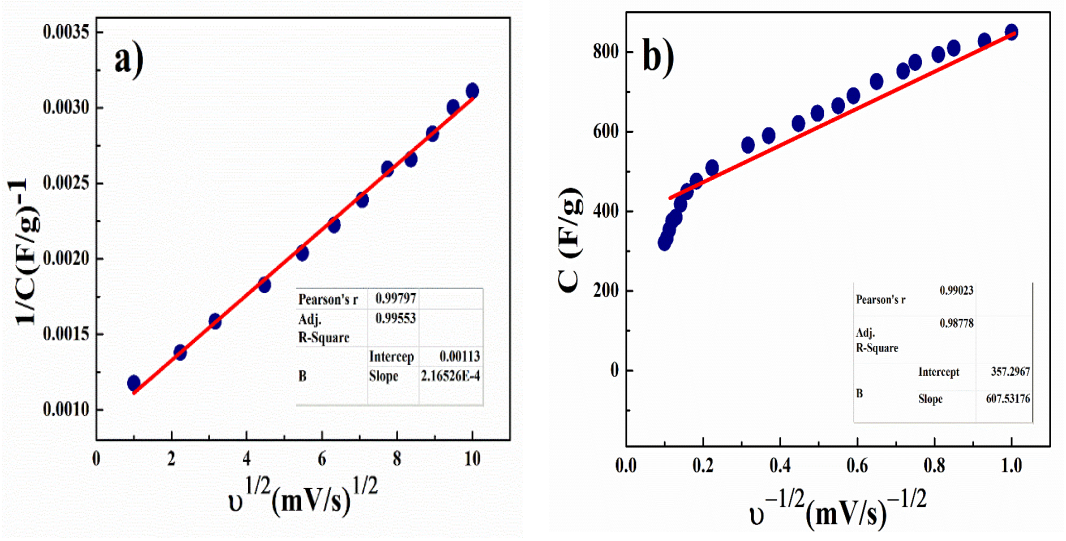


***Figure 4.6:*** *(a-b) Trasatti plot at a scan rate of 100 to 1 mV/s during the charge/discharge reactions.*

**Fig. 4.7(a)** depicts the Galvanostatic capacity/ capacitances of $KNiPO_4$ and the values are found close to 168 mAh/g (capacitances: 935 F/g), 153.5 mAh/g (capacitances: 852 F/g), 137.5 mAh/g (capacitances: 762F/g, 116mAh/g (capacitances: 646F/g), 96.5 mAh/g (capacitances: 535 F/g), and 80.5 mAh/g (capacitances: 446F/g) at the current rates of 1, 2, 3, 4, 5 and 10A/g. With the increase in current rates, the charge storage capacity of the material decreased. The charge storage capacity decreases to 55% of its initial value in the change of current density from 1 A/g to 10A/g.

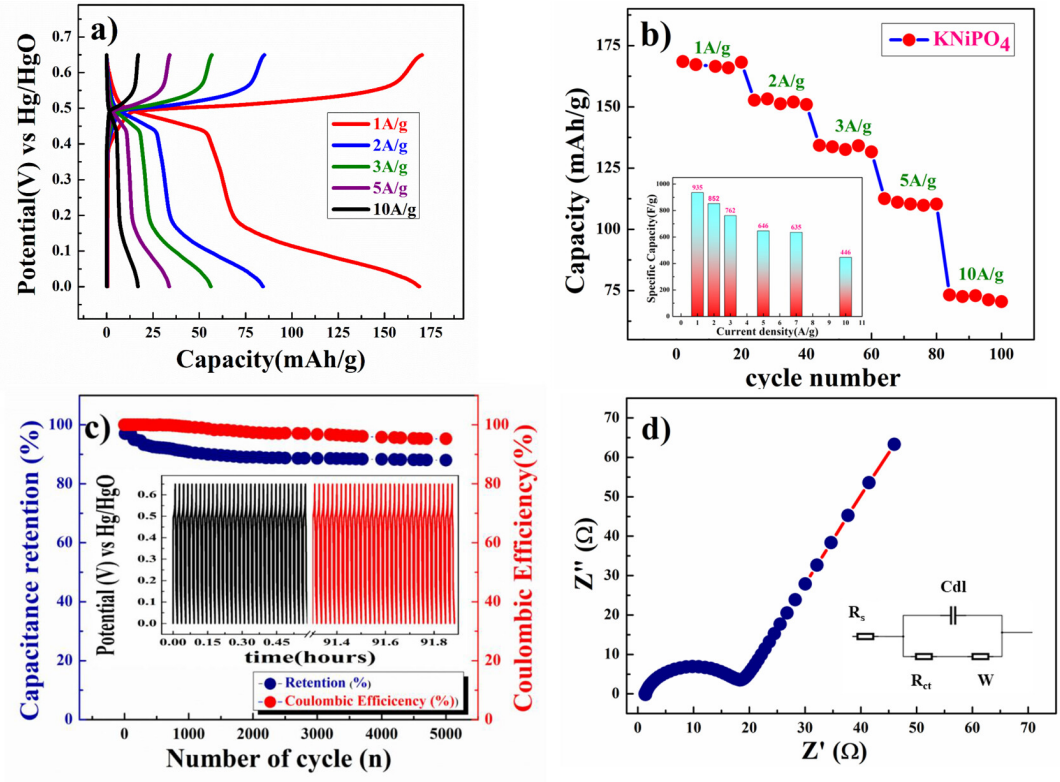


***Figure 4.7.*** *(a) Charge/discharge plot (V vs time) of the $KNiPO_4$ electrode at various constant current rates ( 1, 2, 3, 5, and 10 A/g), (b) capacity/capacitance performance of the $KNiPO_4$ in 2 M KOH electrolyte at different current densities, (c) Capacity retention and Coulombic efficiency plot and (d) impedance spectra at 10 mV applied voltage in the frequency range of 1 MHz to 0.1 Hz.*

**Fig. 4.7(b)** represents the charge storage capacity/ capacitance value of the electrode with cycle numbers at different constant current rates. **Fig. 4.7(c)** presents the superior cycle stability of $KNiPO_4$ electrodes at 10A/g for 5000 cycles. It was observed that 87% of capacity retention after 5000 cycles. Simultaneously, **Fig. 4.7(c)** also displays the

coulombic efficiency ($\eta = {}^{t_d}/_{t_c}$) of the electrode and it was found ~ 95.1 % after 5000 cycles of charge/discharge that suggest the superior reversibility and robust performance of the $KNiPO_4$ electrode.

We also performed AC electrochemical impedance spectroscopy (EIS) shown as Nyquist Plot in **Fig. 4.7(d)** at 10mV of the applied potential in the frequency range(1MHz-0.1Hz). The total impedance contribution was a contribution of electric series resistance (Rs: 1.87Ω), charge transfer resistance (Rct: 16.7Ω), and Warburg impedance (Rw: 70.92Ω). The intercept in the EIS spectra on the real axis was at 1.87 Ω in the high-frequency region indicating very small internal resistance of the electrode. The small semicircle in the high-frequency region also represents the faster rate of charge transport between the electrode and electrolyte and the lower frequency data exhibits the Warburg diffusion resistance of the electrode. The slope linear line of the $KNiPO_4$ electrode in the low-frequency region is close to a 45° angle from the horizontal axis representing the intercalative charge storage (battery type) of the $KNiPO_4$ electrode and fast $OH^-$ ion diffusion in the host structure of the electrode [7].

### 4.3.2 Full cell measurements in Hybrid Supercapacitor (HSC) Mode

To explore the full potential of the $KNiPO_4$ electrode, full cell performance measurement was carried out in two-electrode HSC (hybrid supercapacitor) mode in a 2M KOH electrolyte. To obtain the highest charge storage capacity in the full cell test, the storage capacity of both electrodes was balanced using the equation presented below:

$$\frac{1}{C_{total}} = \frac{1}{C_{positive}} + \frac{1}{C_{negative}} \qquad (4.13)$$

To balance the charge storage capacity of the individual electrode in the cell, the mass ratio ($m^+/m^-$) of both electrodes was calculated using the equation presented below:

$$\frac{m^+}{m^-} = \frac{C_- \times \Delta E_-}{C_+ \times \Delta E_+} \qquad (4.14)$$

Where $m^+, m^-, C_+, C_-, \Delta E_+, \Delta E_-$ are active mass, specific capacitance, and potential window of both electrodes.

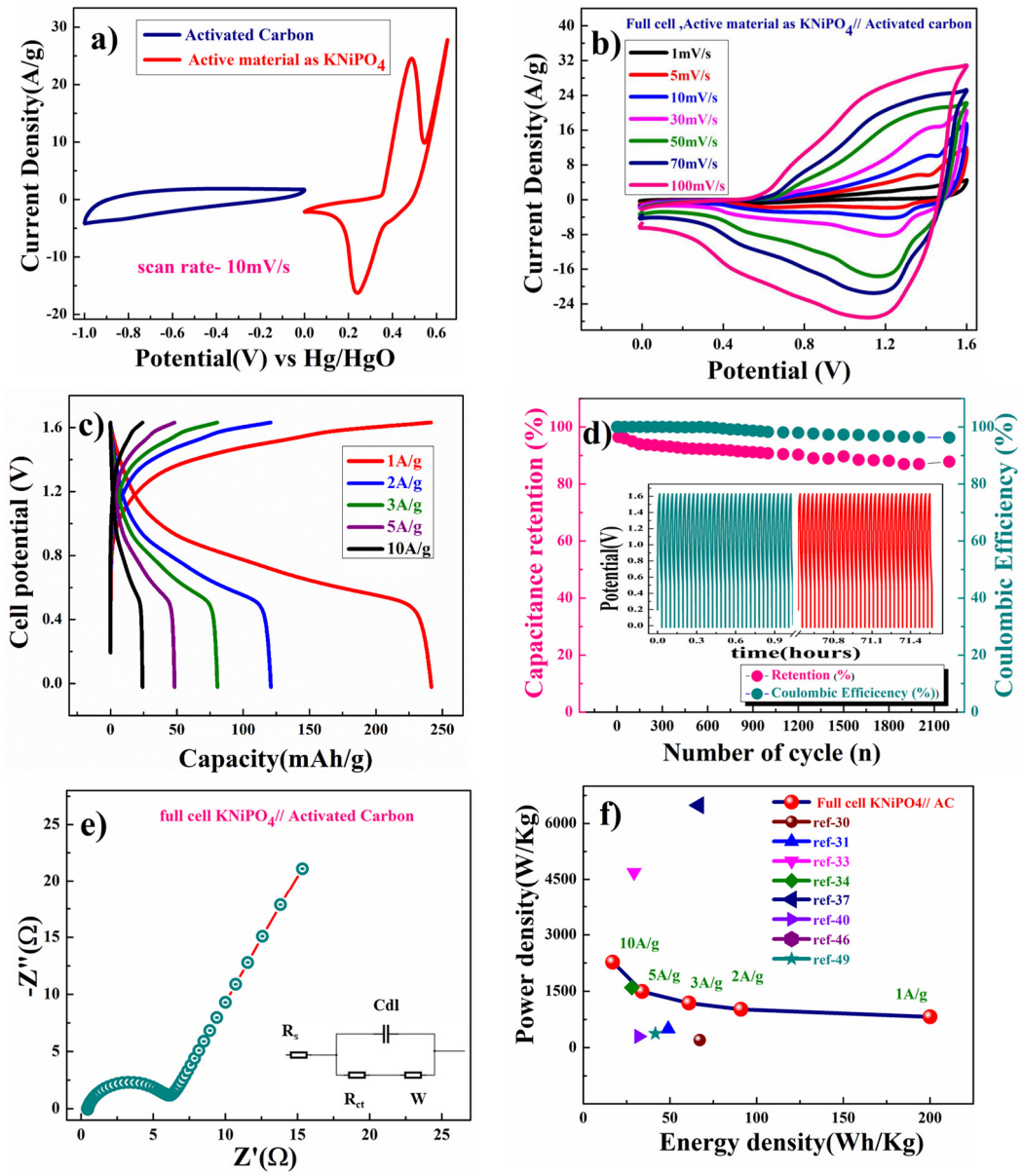


***Figure 4.8***. *Full cell performance in two-electrode Hybrid Supercapacitor (HSc) mode containing $KNiPO_4$ electrode and activated carbon as a positive and negative electrode; (a) CV plot of individual electrodes at the scan rate of 10 mV/s with Hg/HgO as reference electrode, (b) CV of the full cell at different scan rates, (c) charge/discharge profile of full cell at different constant current rates, (d) Impedance spectra of the full cell at 10 mV applied voltage, (e) capacity retention and Coulombic efficiency plot of the full cell at constant current rates of 10 A/g, and (f) Ragone plot of the full cell in HSc mode.*

**Fig. 4.8(a)** shows the independent CVs of AC (activate carbon) (the negative electrode) and $KNiPO_4$ (the positive electrode). The active mass ratio ($\frac{m^+}{m^-}$) of electrodes was found to be 1: 2.97. **Fig. 4.8(b)** demonstrates the CV curve of $KNiPO_4$ //AC full cell in two electrode HSC (Hybrid Supercapacitor) mode in the scan rates of 1mV/s to 100mV/s in the potential window of 1.6V. **Fig. 4.8(c)** subsequently, shows the galvanostatic charge/discharge plot of the full cell to get the actual capacity/ capacitance of the cell. The capacity/capacitance value was calculated was Eq. 10 and the charge storage capacity full hybrid supercapacitor was found to be 242.5 mAh/g (capacitance: 546 F/g), 113.7 mAh/g (capacitance: 256 F/g), 76.5 mAh/g (capacitance: 172 F/g), 48.5 mAh/g (capacitance:109 F/g), and 24.5 mAh/g (capacitance: 55 F/g) at respective current rates of 1A/g, 2A/g, 3A/g, 5A/g, and 10A/g. **Fig. 4.8(d)** presents the EIS spectra (Nyquist plot) in the frequency range (1MHz - 0.1Hz) at 10mV/s of applied potential showing higher charge transfer resulting in the superior capacitive performance of the full cell ($KNiPO_4$ //AC).

**Fig. 4.8(e)** presents the coulombic efficiency plot of two electrode cells and the efficiency was reduced only by 3.4 % with capacity retention close to 92.3 % of its initial value after 2200 cycles of the operations. Charge storage capacity (energy density) and power capacity of full in HSc mode were calculated using the equations presented below:

$$E(Wh/kg) = \frac{1}{2}\frac{C_{ASCs}}{3.6}V^2 \qquad (4.15)$$

$$P(W/kg) = \frac{E*3600}{t_{dis}} \qquad (4.16)$$

Where $C_{ASCs}$ is specific capacitance, V is Potential window and $t_{dis}$ is discharge time [18, 19].

**Fig. 4.8(f)** presents an energy density vs power capacity plot at different constant current densities. Full cell shows the highest energy density equal to 200 Wh/kg at 1 A/g current rates achieving power capacity close to 819W/kg. The highest power capacity equal to 2273

W/kg was obtained at an energy density close to only 17 Wh/kg at a current density of 10 A/g for the full cell. These superior full-cell performances of the $KNiPO_4$ electrode in two-electrode HSc mode confirm the applicability of developed $KNiPO_4$ electrodes in developing superior hybrid supercapacitors.

## 4.4 Conclusions

In summary, $KNiPO_4$ was successfully synthesized using a two-step process utilizing a modified solution combustion process followed by calcination at elevated temperatures. The amorphous powder prepared by a modified solution combustion process was calcined at 650$^oC$ for 5 hours to result in the formation of crystalline $KNiPO_4$. The KNiPO4 electrodes exhibited an energy density/capacitance equal to 168.5 mAh/g (Capacitance: 935 F/g) at 1 A/g current density with excellent cyclic stability. In **Table 4.1,** we provided comparative performances of other phosphate base transition metal phosphate-containing electrodes in Hybrid Supercapacitor (HSc) mode. The predominant intercalative pseudocapacitive charge storage behavior seems to be the reason behind the high capacitance of the electrode due to the active involvement of $Ni^{2+/3+}$ redox couple mediate charge storage as intercalative (inner) and capacitive, (outer) surface charges storage on the electrode were close to 58% and 42% respectively. $KNiPO_4$ electrodes exhibit excellent long-term cycle stability at 10A/g for 5000 cycles with 87% of the electrode`s initial capacity retention and coulombic efficiency ($\eta = {}^{t_d}/_{t_c}$) equivalent to 95.1 % after 5000 cycles.

| **Materials** | **Energy density/ Power density** | **Capacitance/ capacity** | **Electrolyte** | **References** |
|---|---|---|---|---|
| $Ni_3(PO4)_2$ @GO | ED= 67.2 Whkg$^{-1}$ at PW= 200.43 W kg$^{-1}$ | 1392.59 F g$^{-1}$ at 0.5 A g$^{-1}$ | 2 M KOH | [20] |
| $Ni_3(PO_4)_2$ @ graphene foam | ED=49 W h kg$^{-1}$ at PW= 499 W kg$^{-1}$ | 48 mA h g$^{-1}$ at 0.5 A g$^{-1}$ | 6 M KOH | [21] |
| $Co_3(PO4)_2 \cdot 8H_2O$ | ED= 29.29 Wh kg$^{-1}$ PW=4687 W kg$^{-1}$ | 1578.7 F g$^{-1}$ at 5 mA cm$^{-2}$ | 1 M NaOH | [22] |
| γ-$KCoPO_4$ | ED= 28 W h kg-$^{1}$ at PD=1600 W kg$^{-1}$ | 100 C g$^{-1}$ at 0.6 mA cm$^{-2}$ | 1 M KOH | [23] |
| $KFePO_4$ | ----- | 90 mAh g$^{-1}$ at 10 mA g$^{-1}$ | $KPF_6$ in EC /DEC | [24] |
| $NaFe_2PO_4(SO_4)_2$ | ----- | 90 mAh g$^{-1}$ at 0.1C | 1M $NaClO_4$ in 10% | [25] |
| $CoNiP_2O_7$ | ED=66.7 Wh kg$^{-1}$ at PW= 6486.5 W kg$^{-1}$ | 136.2 mAh g$^{-1}$ at 1 A g$^{-1}$ | $LiPF_6$ in EC/DMC/EM | [26] |
| $Na_3Cr_2(PO4)_3$ | ----- | ~98 mAh g$^{-1}$ at 0.5 C | 1 M NaPF6 EC/ DC | [27] |
| $Na_3V_2(PO_4)_3$/C | ----- | 108.5 mAh/g at C/10 | NaFSI/PC | [28] |
| $NaNiPO_4$ | ED= 32 W h kg$^{-1}$ at PD= 300 W kg$^{-1}$. | 345 F g$^{-1}$ | 2 M NaOH | [29] |
| $LiNiPO_4$ | ----- | 55 mAh/g | LiOH pH - 10.5 | [30] |
| MP-$VOPO_4$@rGO | ED- 108 Wh kg$^{-1}$ | 527.9 F g$^{-1}$ at 0.5 A g$^{-1}$ | 6 M KOH | [31] |
| $NaTi_2(PO_4)_3$ | ------- | 131.2 mAh/g at 0.1C | $NaClO_4$ in EC/DC | [32] |
| $Ni_2P_2O_7$/$Co_2P_2O_7$ | ED =33.1 Whkg$^{-1}$ PD= 257.7 Wkg−1 | 2074Fg$^{-1}$ at 5Ag$^{-1}$ | 2 M KOH | [33] |
| $Na_3Fe_2(SO_4)_2PO_4$ | ----- | 70 mA h g$^{-1}$ at C/10 | 1M $NaPF_6$ in EC/PC | [34] |

| | | | | |
|---|---|---|---|---|
| $KCo_{0.33}Ni_{0.67}PO_4 \cdot H_2O$ | ED= 8 000 $Wkg^{-1}$ at PW=80.64 $Whkg^{-1}$ | 178 mA h $g^{-1}$ (1166 F $g^{-1}$) at 1.5 A $g^{-1}$ | 1 M KOH | [35] |
| LiCoPO4/C | ------ | 123 mAh $g^{-1}$ at C/10 | 1M LiPF/EC +DMC+EMC | [36] |
| $LiMnPO_4$/C | ------ | 155 mA h $g^{-1}$ at 0.5 C | 1M LiPF6/EC +DMC+EMC | [37] |
| $NH_4NiPO_4 \cdot H_2O$ | ED= 41.6 Wh $kg^{-1}$ at PD= 375 W $kg^{-1}$ | 1513 F $g^{-1}$ at 5 A $g^{-1}$ | 3M KOH | [38] |
| $NaVOPO_4$ | ------ | 90 mA h $g^{-1}$ at 1/15 C | 1 M NaClO4 in PC | [39] |
| $Mo_2P_2O_{11}$ | ----- | 89mAh/g at C/10 | 1 M NaClO4 in FEC/PC | [40] |
| **$KNiPO_4$** | **ED=200 Wh/kg PD=819 W/kg** | **168.5 mAh/g Capacitance: 935 F/g) at 1 A $g^{-1}$** | **2M KOH** | **Present Work** |

***Table 4.1****: A comparative study of electrochemical performances of transition metal phosphate containing polyanionic framework structure-based electrode materials*

The $KNiPO_4$ //AC full cell in HSc mode achieved the highest energy density close to 200 Wh/kg with a power capacity reaching 819 W/kg in the potential window of 1.6V in 2M KOH electrolyte. The full cell in HSc mode also showed a very high-power capacity close to 7981 W/kg attaining a charge storage capacity equivalent to 75 Wh/kg at the current rate of 10 A/g with superior cyclic stability. Coulombic efficiency of the full Cell (ASC mode) has lost only 3.4 % with excellent capacity retention (92.3 %) of its initial value after 2200 cycles. The robust performance and long cycle life of the electrode in full cells confirm the applicability of the material to power biomedical devices.

## References


1. Wang, M. Y.; Zhao, X. X.; Guo, J. Z.; Nie, X. J.; Gu, Z. Y.; Yang, X. & Wu, X. L. Enhanced electrode kinetics and properties via anionic regulation in polyanionic $Na_{3+x}V_2(PO_4)_{3-x}(P_2O_7)_x$ cathode material. Green Energy and Environment, **2022**, 7, 4, 763-771. 32 old

2. N.Priyadharsiniab, R.Kalai Selvan. Nano-sheet-like KNiPO4 as a positive electrode material for aqueous hybrid supercapacitors, Electrochimica Acta , **2017**, 246, 963-970

3. Essehli, R.; El Bali, B.; Benmokhtar, S.; Fuess, H.; Svoboda, I. and Obbade, S. Synthesis, crystal structure and infrared spectroscopy of a new non-centrosymmetric mixed-anion phosphate $Na_4Mg_3(PO_4)2(P_2O_7)$. *Journal of Alloys and Compounds*, **2010**, 493, (1–2), 654–660.

4. Kosova, N. V.; Belotserkovsky, V. A. Sodium and mixed sodium/lithium iron ortho-pyrophosphates: Synthesis, structure and electrochemical properties. *Electrochimica Acta*, **2018**, 278, 182–195.

5. Xu, L.; Zhang, J.; Ding, J.; Liu, T.; Shi G.; Li, X.; Dang, W.; Cheng Y.; Guo, R. Pore Structure and Fractal Characteristics of Direcent Shale Lithofacies in the Dalong Formation in the Western Area of the Lower Yangtze Platform, Minerals, **2020**, 10,1, 72.

6. Li, J.-J.; Liu, M.-C.; Kong, L.-B.; Wang, D.; Hu, Y.-M.; Hanband, W.; Kang, L. Advanced asymmetric supercapacitors based on $Ni_3(PO_4)_2$@GO and $Fe_2O_3$@GO electrodes with high specific capacitance and high energy density, RSC Adv., **2015**, 5, 41721.

7. Mishra, N. K.; Singh, A. K.; Mondal, R.; Singh, P.; $NiC_2O_4{\cdot}2H_2O$ Nanoflakes: A Novel Redox-mediated Intercalative Pseudocapacitive Electrode for Supercapacitor Applications in Aqueous KOH and Neutral $Na_2SO_4$ electrolytes, **2022**, 7, 21, e202201134

8. Mondal, R.; Mishra, N. K.; Maiyalagan, T.; Gupta, A.; Singh, P. $La_{1-x}K_xFeO_{3-\delta}$: An Anion Intercalative Pseudocapacitive Electrode for Supercapacitor Application, ACS Omega **2021**, 6, 30488−30498.

9. Lang, X.; Mo, H.; Hu, X.; Tian, H. Supercapacitor performance of perovskite $La_{1-x}Sr_xMnO_3$, *Dalton Trans*. 2017, 46, 13720−13730.

10. Gupta, A.; Kushwaha, V.; Mondal, R.; Singh, A. N.; Prakash, R.; Mandal, K. D. and Singh, P. $SrFeO_{3-\delta}$: a novel $Fe^{4+}$ to $Fe^{2+}$ redox-mediated pseudocapacitive electrode in aqueous electrolyte, *Phys. Chem. Chem. Phys*., 2022, 24, 11066.

11. Wang, X.; Sumboja, A.; Lin, M.; Yan J. and Lee, P. S. Enhancing electrochemical reaction sites in nickel-cobalt layered double hydroxides on zinc tin oxide nanowires: a hybrid material for an asymmetric supercapacitor device, *Nanoscale*, **2012**, 4, 7266.

12. Kumar R. and Bag, M. Quantifying Capacitive and Diffusion-Controlled Charge Storage from 3D Bulk to 2D Layered Halide Perovskite-Based Porous Electrodes for Efficient Supercapacitor Applications, *J. Phys. Chem. C* ,**2021**, 125, 16946−16954.

13. Wang, K.; Wang, S.; Liu, J.; Guo, Y.; Mao, F.; Wu, H. and Zhang, Q. Fe-Based Coordination Polymers as Battery-Type Electrodes in Semi-Solid-State Battery−Supercapacitor Hybrid Devices, *ACS Appl. Mater. Interfaces,* **2021**, 13, 15315−15323.

14. Huang, J.; Yuan, K.; Chen, Y. Wide Voltage Aqueous Asymmetric Supercapacitors: Advances, Strategies, and Challenges, Adv. Funct. Mater. **2022**, 32, 2108107.

15. Brousse, T.; B´elanger, D. and Longd, J. W. To Be or Not To Be Pseudocapacitive? Journal of The Electrochemical Society, **2015**, 162 (5) A5185-A5189.

16. Augustyn, V.; Come, J.; Lowe, M. A.; Kim, J. W.; Taberna, P.-L.; Tolbert, S. H.; Abruña, H. D.; Simon P. and Dunn B. High-rate electrochemical energy storage through Li+ intercalation pseudocapacitance. Nat. Mater. **2013**, 12, 518–522.

17. Wang, J.; Polleux, J.; Lim, J.; Dunn, B. Pseudocapacitive Contributions to Electrochemical Energy Storage in $TiO_2$ (Anatase) Nanoparticles, *J. Phy. Chem. C*, **2007**, 111, 14925-14931.

18. Mishra, N. K.; Mondal, R.; Maiyalagan, T.; Singh, P. Synthesis, Characterizations, and Electrochemical Performances of Highly Porous, Anhydrous $Co_{0.5}Ni_{0.5}C_2O_4$ for Pseudocapacitive Energy Storage Applications, ACS Omega 2022, 7, 1975−1987.

19. Zhang, G.; Li, Y.; Xiao, X.; Shan, Y.; Bai, Y.; Xue, H. G.; Pang, H.; Tian, Z. and Xu, Q. In Situ Anchoring Polymetallic Phosphide Nanoparticles within Porous Prussian Blue Analogue Nanocages for Boosting Oxygen Evolution Catalysis, Nano Lett. 2021, 21, 3016−3025

20. Li, J.-J.; Liu, M.-C.; Kong, L.-B.; Wang, D.; Hu, Y.-M.; Hanb W. and Kangb, L. Advanced asymmetric supercapacitors based on $Ni_3(PO_4)_2$@GO and $Fe_2O_3$@GO electrodes with high specific capacitance and high energy density, RSC Adv., **2015**, 5, 41721.

21. Mirghnia, A. A.; Maditoa, M. J.; Oyedotuna, K. O.; Masikhwaa, T. M.; Ndiayea, N. M.; Rayb S.. J. and Manyala, N. A high energy density asymmetric supercapacitor

utilizing a nickel phosphate/graphene foam composite as the cathode and carbonized iron cations adsorbed onto polyaniline as the anode, RSC Adv., 2018,8, 11608-11621

22. Shao, H.; Padmanathan, N.; McNulty, D. O′Dwyer, C. and Razeeb, K.M. Supercapattery Based on Binder-Free $Co_3(PO_4)_2 \cdot 8H_2O$ Multilayer Nano/Microflakes on Nickel Foam, ACS Appl. Mater. Interfaces **2016**, 8, 28592−28598.

23. Priyadharsini, N.; Surendran, S.; Senthilkumar, B.; Vasylechko, L.; Selvan, R. K. Synthesis and Electrochemical Performances of γ-$KCoPO_4$ Nanocrystals as Promising Electrode for Aqueous Supercapatteries, ehem electro chem, **2019**,6, 2, 369-377.

24. Sultana, I.; Rahman, M. M.; Mateti, S.; Sharma, N.; Huang, S.; Chen, Y. Approaching Reactive $KFePO_4$ Phase for Potassium Storage by Adopting an Advanced Design Strategy, batteries and supercaps, **2020**, 3, 5, 450-455.

25. Shiva, K.; Singh, P.; Zhou, W.; Goodenough, J. B. $NaFe_2PO_4(SO_4)_2$: A potential cathode for a Na-ion battery, Energy Environ. Sci., **2016**,9, 3103-3106.

26. Li, F.-F.; He, Z.-H.; Gao, J.-F.; Kong, L.-B. The investigations of pyrophosphate $CoNiP_2O_7$ produced by hydrothermal process: a high-performance anode electrode material for Li-ion hybrid capacitor, Ionics 2020, 26:2989–3001.

27. Kawai. K, Zhao.W, Nishimura.S, and Yamada.A, High-Voltage Cr4+/Cr3+ Redox Couple in Polyanion Compounds, ACS Appl. Energy Mater. **2018**, 1, 928−931

28. Zelang Jian, Wenze Han, Xia Lu, Huaixin Yang, Yong-Sheng Hu, Jing Zhou, Zhibin Zhou, Jianqi Li, Wen Chen, Dongfeng Chen, Liquan Chen, Superior Electrochemical Performance and Storage Mechanism of $Na_3V_2(PO_4)_3$ Cathode for Room-Temperature Sodium-Ion Batteries, *Advanced Energy Materials*, **2013**,3,2,156-160

29. Sundaram. M. M, Mitchell, D. R. G. Dispersion of $Ni^{2+}$ ions: Via acetate precursor in the preparation of $NaNiPO_4$ nanoparticles: Effect of acetate vs. nitrate on the capacitive energy storage properties. *Dalton Transactions*. **2017**, 46, 40, 13704-13713.

30. Minakshi, M.; Singh, P.; Appadoo, D. and Martin, D. E. Synthesis and characterization of olivine $LiNiPO_4$ for aqueous rechargeable battery, Electrochimica Acta , **2011**, 56 ,4356–4360

31. Lee, K. H.; Lee, Y-W.; Lee, S. W.; Ha, J. S. and Son, J. G. Ice-templated Self-assembly of VOPO4–Graphene Nanocomposites for Vertically Porous 3D Supercapacitor Electrodes. Sci Rep, 2015, 5, 13696

32. Yang , J.; Wang, H.; Hu, P.; Qi, J.; Guo, L. and Wang, L. A High-Rate and Ultralong-Life Sodium-Ion Battery Based on $NaTi_2(PO_4)_3$ Nanocubes with Synergistic Coating of Carbon and Rutile TiO, small ,2015, 11, 31 , 3744-3749

33. Matheswaran, P.; Karuppiah, P.; Chen, S. M. and Thangavelu, P. A binder-free Ni2P2O7/Co2P2O7 nanograss array as an efficient cathode for supercapacitors, New J. Chem., 2020,44, 13131-13140

34. Kumar, S; Ranjeeth, R.; Mishra, N. K.; Prakash, R. and Singh, P. NASICON-structured $Na_3Fe_2PO_4(SO_4)_2$ : a potential cathode material for rechargeable sodium-ion batteries. ***Dalton Trans.*****, 2022, 51,** 5834-5840.

35. Liang, B.; Chen, Y.; He, J.; Chen, C.; Liu, W.; He, Y.; Liu, X.; Zhang, N. and Roy, V. A. L. Controllable Fabrication and Tuned Electrochemical Performance of Potassium Co−Ni Phosphate Microplates as Electrodes in Supercapacitor, ACS Appl. Mater. Interfaces **2018**, 10, 3506−3514

36. Liu, J.; Conry, T. C.; Song, X.; Yang, L.; Doeff, M. M. and Richardson, T. J. Spherical nanoporous $LiCoPO_4$/C composites as high performance cathode materials for rechargeable lithium-ion batteries, J. Mater. Chem., **2011**, 21, 9984-9987

37. Zhu, J. N.; Li, W. C.; Cheng, F.; Lu, A. -H. Synthesis of $LiMnPO_4$/C with superior performance as Li-ion battery cathodes by a two-stage microwave solvothermal process. J. Mater. Chem. A , **2015**, 3 ,26, 13920−13925

38. Chen, C.; Zhang, N.; Liu, X.; He, Y.; Wan, H.; Liang, B.; Ma, R.; Pan A. and Roy, V. A. L. Polypyrrole-Modified NH4NiPO4•H2O Nanoplate Arrays on Ni Foam for Efficient Electrode in Electrochemical Capacitors, ACS Sustainable Chem. Eng. 2016, 4, 10, 5578–5584

39. Song, J.; Xu, M.; Wang, L. and Goodenough, J. B. Exploration of $NaVOPO_4$ as a cathode for a Na-ion battery, Chem. Commun., **2013**, 49, 5280

40. Kumar, S.; Singh, M.; Mondal, R.; Singh, M.; Prakash, R. and Singh, P. $Mo_2P_2O_{11}$: A Potential Cathode Material for Rechargeable Sodium-Ion Batteries, Energy Fuels ,**2023**, 37, 1288−1296